Journal of Materials Chemistry A

COMMUNICATION

View Article Online
View Journal | View Issue

Atmospheric growth and strong visible luminescence of anatase titanium oxide films with various orientations†

Cite this: J. Mater. Chem. A, 2014, 2, 6708

Received 11th February 2014
Accepted 14th March 2014

DOI: 10.1039/c4ta00730a

www.rsc.org/MaterialsA

M. L. Li,[ab] G. S. Huang,*[b] D. X. Wang,[a] J. Zhang,*[a] J. J. Shi[a] and Y. F. Mei[b]

At atmospheric pressure, anatase TiO_2 films with various nanomorphologies have been grown on quartz substrate by non-thermal $TiCl_4$–O_2–Ar reactive plasma vapor deposition. High concentration of oxygen vacancies and undercoordinated Ti atoms are incorporated into the crystal lattice of the deposited films, which can be tuned by changing the discharge conditions such as temperature and vapor flow rate. Strong visible luminescence is found for the deposited films, originating from the radiative recombination of trapped electrons due to uncoordinated Ti atoms and oxygen vacancies. To clarify the growth mechanism, an analytical model is proposed to explain the corresponding discharging process. We find the theoretical predictions agree well with experimental results. By effectively adjusting the morphology and lattice crystallinity, we believe this work can provide an expedient and controllable way to fabricate anatase films with interesting optical properties, which can meet the demands of complex practical situations to the maximum degree.

Introduction

Titanium dioxide (TiO_2) is an industrially important wide-band gap semiconductor with plenty of applications in a wide range of technological fields such as heterogeneous catalysis, photoelectrolysis, biocompatibility, and sanitary disinfection,[1–5] which have spurred a great deal of research focused on its bulk structures and surface properties. Owing to the advantages of some special facets of TiO_2, which are related to its unique lattice properties and widely applied to fields like the photocatalytic process,[6,7] it is believed that there is great necessity to emphasize the importance of TiO_2 nanostructures fabricated with certain crystal structures. For instance, anatase TiO_2 exhibits a higher activity than other polymorphs and has been generally used for renewable energy development and in biomedical areas.[8,9]

The {101} facet of anatase TiO_2 has always attracted attention because it is favorable to most practical situations mainly due to its thermodynamic stability. As predicted previously, the most stable form of the anatase polymorph is a tetragonal bipyramidal structure in which {101} facets are primarily exposed (more than 94%), with a small percentage of {001} facets.[10] On the other hand, anatase {001} facet is also found to be beneficial since a crystal with these surfaces exhibits high carrier mobility, low incident light reflection loss, and large reactive surfaces.[11,12] However, the highly reactive facets can hardly survive in complex situations and will diminish rapidly during crystal growth due to the minimization of surface energy.[13] Much attention has also been paid to the tuning of the lattice structure to minimize the energy loss of the high-energy {001} facet, among which the methods involving fluorine are mentioned frequently.[14,15] According to the recent results of Yang *et al.*,[16] the introduction of hydrofluoric acid (HF) during the hydrothermal synthesis of TiO_2 can stabilize the {001} facet, allowing for the formation of truncated bipyramidal structures in the micrometer size range. Nevertheless, such a method can only enhance the percentage of {001} facets to 47% and has met with a lot of difficulties in further improvement. Other attempts such as plasma-assisted molecular beam epitaxy, ion implantation, and electron bombardment, which are expected to induce the formation of anatase {101} and {001} facets, however, suffered from the annihilation of the high-energy surface and from lattice disorder led by the constant disturbance of newly formed oxygen vacancies (OVs).[17–20] Furthermore, it has been reported that specific lattice defects are selectively introduced into the TiO_2 structure in applications like photocatalysis, photoconversion and gas sensing.[21–23] For example, Ti^{3+} can help to form a microstructured composite between hydrophilic and oleophilic phases, which will finally enhance the photoconvertible surface wettability.[24] Wang *et al.* reported the effect of OVs and hydrogen treatment to help increase the donor density of TiO_2 nanowires by three orders of magnitude and

[a]College of Science, State Key Laboratory for Modification of Chemical Fibers and Polymer Materials, College of Materials Science and Engineering, Donghua University, Shanghai 201620, People's Republic of China. E-mail: jingzh@dhu.edu.cn
[b]Department of Materials Science, Fudan University, Shanghai 200433, People's Republic of China. E-mail: gshuang@fudan.edu.cn

† Electronic supplementary information (ESI) available: Additional SEM and TEM images of the TiO_2 films. See DOI: 10.1039/c4ta00730a

finally enhance the photocurrent of TiO_2 under UV exposure.[25] Therefore, it is a challenge to produce TiO_2 structures with designed lattice orientation and demanded defects so as to meet the requirements of various applications.

In this work, anatase TiO_2 film with controllable orientation along (101) or (001) was fabricated by an atmospheric discharge process without the use of any catalysts or templates. Strong photoluminescence emission can be seen when the deposited film is excited by a laser, which can be mostly ascribed to the effect of OVs and uncoordinated Ti atoms. The experimental results demonstrate a complex growth process, and we found that the lattice structure of the anatase TiO_2 can be altered by changing the reaction temperature and the precursors' concentrations. The method used in this work is compatible with mass production in industrial manufacturing, and therefore can be widely adopted in the future.

Experimental

Atmospheric pressure non-thermal reactive plasma of a $TiCl_4$–O_2–Ar mixture was applied to produce TiO_2 film. The plasma-enhanced chemical vapor deposition (PECVD) process took place in a home-made atmospheric pressure plasma reactor composed of two coaxial quartz tubes with a gap of 1.5 mm. A 13.56 MHz radio-frequency power supply was applied to ignite the plasma in the space between the two electrodes (I) and (II), as shown in Fig. 1(a). $TiCl_4$–O_2–Ar mixture was fed into the reactor through mass flow controllers and the anatase TiO_2 film was obtained directly on the quartz substrate placed in the chamber after 1–2 h without any post-treatments. During the discharging process, the temperature of the reactor was monitored by thermocouples. The morphology and crystal structure of the deposited film were examined using field emission scanning electron microscopy (FE-SEM, S-4800, Hitachi), transmission electron microscopy (TEM, JEM-2010, JEOL), and X-ray diffraction (XRD, D/max-2550 PC, Rigaku). X-Ray photoelectron spectroscopy (XPS, PHI 5000C ESCA) was used to examine the lattice defects in the film. A 325 nm He–Cd laser with pump power of 30 mW was used as excitation source to measure the photoluminescence (PL) spectra of the samples in order to investigate the optical properties.

Results and discussion

Fig. 1(a) is a schematic representation illustrating the deposition process. A quartz substrate was placed into the reactor to collect the TiO_2 film formed close to the cathode. The introduced reactive plasma of $TiCl_4$–O_2–Ar gradually spread into the whole atmosphere and was then decomposed into various species including TiO_2Cl_3, O_2, O, Cl, Cl_2, and ClO, which all contribute to the formation of TiO_2 through the overall reaction:

$$TiCl_4 + O_2 \xrightarrow{\text{plasma}} TiO_2 + 2Cl_2$$

From a typical SEM image shown in the left inset of Fig. 1(b), one can see the sample is a film consisting of uniform small

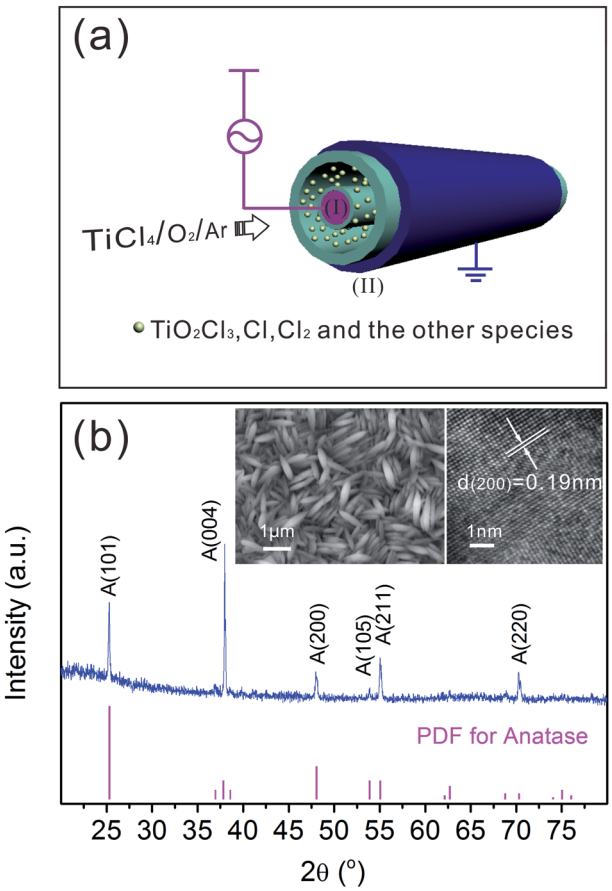

Fig. 1 (a) Schematic representation of the fabrication process of anatase TiO_2 film. (b) A typical XRD pattern of the fabricated sample. A: anatase. The left and right insets show corresponding SEM and HRTEM images respectively.

grains of diamond shape with large aspect ratio. To check the crystal structure of the sample deposited on substrate, we carried out XRD measurement and the results are shown in Fig. 1(b), and all the direction peaks in the XRD pattern can be well indexed to anatase TiO_2 (see the peak positions from standard PDF database). Importantly, the relative intensities of the diffraction peaks obviously suggest a partially preferential growth direction of TiO_2 along the (004) direction. The HRTEM characterization also demonstrated clear lattice fringes with a distance of 0.19 nm (from (200) lattice plane of anatase TiO_2), as shown in the right inset of Fig. 1(b). The HRTEM image further confirms the formation of anatase phase with good crystal quality.

It is natural to know that the distribution of plasma inside the chamber cannot be completely uniform. This was proven by normal photography of the discharge glow in the plasma reactor. Fig. 2(a) shows a photograph of the cross-sectional view of the reactor during plasma discharge. The glow between the two quartz tubes is brilliant and almost homogeneous due to the central symmetry. However, the photograph of the lateral view of the reactor (Fig. 2(b)) shows the glow is not uniform along the reactor axis: the glow in the middle part is much brighter than that near the edge. An in-depth analysis was

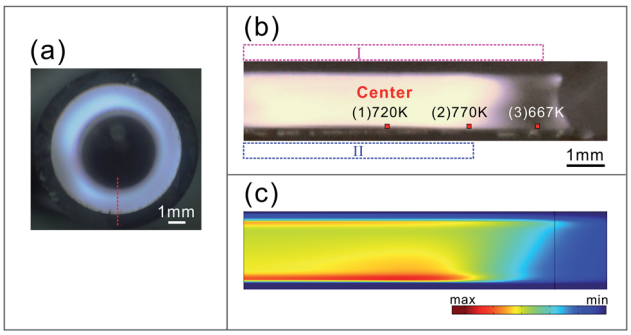

Fig. 2 (a) Photograph of the plasma reactor during the discharge process (cross-sectional view perpendicular to the axis). (b) Photograph of the lateral view of the plasma reactor during the discharge process: (1) the in-glow discharge zone, (2) the boundary zone, and (3) the afterglow discharge zone. The lateral view of the reactor in (b) corresponds to the red dashed line in (a). (c) Simulated electron density in the reactor. The geometry is the same as that in (b).

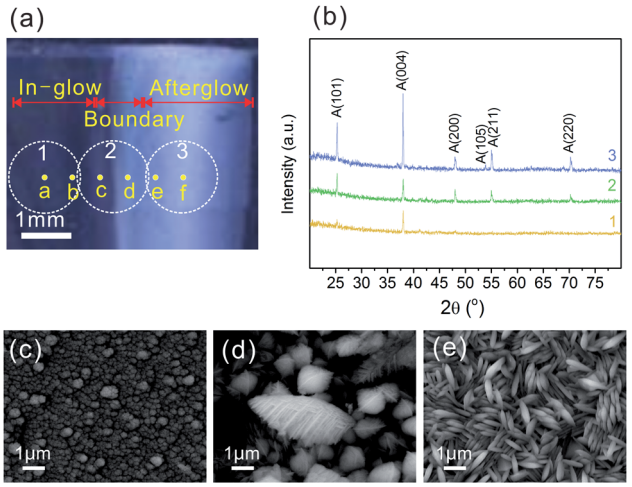

Fig. 3 (a) A photograph of TiO_2 film fabricated by PECVD process. Film with in-glow, boundary, and afterglow zones labelled. Samples from three testing spots were selected for further characterization: spot 1 is located in the in-glow zone, spot 2 is in the boundary zone, and spot 3 is in the afterglow discharge zone. (b) XRD patterns of samples taken from the three test points marked in (a). A: anatase. (c–e) The corresponding SEM images of the samples from the three test spots (1–3) mentioned in (a).

carried out with the help of theoretical simulation. Fig. 2(c) shows the corresponding simulated electron density during plasma discharge (lateral view corresponds to Fig. 2(b)). The simulated results agree well with the experimental results, and on the basis of the electron density (glow intensity) distribution, the chamber can be roughly divided into three regions: (1) the in-glow discharge zone is depicted as the section at the center of the reactor and suffers from the most severe plasma attack; (2) the boundary area describes the area around the edge of the cathode where the ions are not so crowded as in the in-glow discharge zone; and (3) the afterglow zone is the part which does not encounter the main ion flow and is located in the end of the apparatus. Obviously, the ions are mostly collected in the in-glow discharge zone in which a bright light is emitted. The temperatures of different regions during the discharge have also been obtained as evidence of the successive changes happening in the reactor. It is detected that, although no exterior heating device was used, the boundary section reached the highest temperature (770 K) by a self-heating process and temperatures of the in-glow discharge and the afterglow discharge zones are only 720 and 667 K, respectively. The differences in plasma intensity and temperature, which originate from the radio-frequency power supply and corresponding electromagnetic field, should significantly influence the film deposition and thus need to be carefully investigated. The substrate as well as the sample in the in-glow section experience more ion attacks while the substrate/sample located in the afterglow section only suffers from a small number of collisions and such a difference should produce TiO_2 structures with different morphological features, which will be discussed in detail in the following sections.

A quartz substrate was placed into the chamber which runs through all of the three zones and therefore is able to obtain complete information of samples formed at different regions in one deposition. A photograph of the substrate with samples deposited is presented in Fig. 3(a). The difference in film formed is noticeable even to the naked eye. The TiO_2 which grew in moderate atmosphere (the afterglow zone) has formed a thick film, while in the region with intense ion attack (the in-glow zone) one can only see a very thin film. Here, to probe the difference more specifically, we took three typical samples from in-glow zone, boundary zone, and afterglow zone (see spots 1, 2, and 3 respectively in Fig. 3(a)). Typical SEM images of these three samples are shown in Fig. 3(c)–(e), respectively. We found that the largest crystal grains are formed in the boundary zone where the highest temperature was achieved (see also Fig. 2). This result accords with previous literature in which high temperature is confirmed to be beneficial for crystal growth.[26] The kinetic process of crystal growth suggests that the higher the intermediate primary precursor density and the temperature, the higher the crystal growth rate and the higher the crystal lattice regularity.[27] Thus the anatase crystal grown in the boundary zone is confirmed to be large but less uniform. When it comes to the afterglow discharge zone, grains became smaller because the concentration of plasma drops dramatically in this zone. On the other hand, even smaller crystals are observed in the in-glow zone (spot 1). The phenomenon is not hard to understand, since there is no time for plasma to form big crystal grains before the ions in the in-glow zone destroy them. In addition to the morphology evolution, the structural properties of the samples are also different. In order to probe the structural properties of the samples, XRD patterns of the three spots were collected and are exhibited in Fig. 3(b). All of the diffraction peaks shown prove the existence of only anatase TiO_2 in the three samples. In general, diffraction peaks are weak for the sample from spot 1 (in-glow zone) and are much stronger for the sample from spot 3 (afterglow zone), probably due to the larger thickness of the film at spot 3. However, some specific diffraction peaks appear to be more obvious than others for certain samples. Anatase (101) and (004) peaks are the two dominant

peaks shown in the patterns and therefore are chosen for further discussion. Careful comparison has been made and we discover that both the integral area and the height ratio of these two peaks for different samples experience visible fluctuation. For the samples from in-glow and afterglow discharge zones, (004) peak has higher intensity than (101) peak, while they possess similar intensities for the sample from the boundary zone. The difference in the intensities of the XRD peaks, *i.e.* the different crystal structures, should be mainly due to the variable temperatures in the plasma discharge. The increased temperature in the boundary zone largely activated the ions and the film finally tends to form a stable facet with lower surface energy.[28]

PL spectroscopy as a highly sensitive technique to detect the structural properties of TiO_2 crystals.[29] Herein we tried to study the structure of the TiO_2 films in more detail by investigating their light emission properties. To achieve this, we selected six small spots (spots a–f; diameter: ~2 μm) between spots 1 and 3 in Fig. 3(a) with equal spacing and measured corresponding PL spectra. The broad PL peaks clearly demonstrate that luminescent defects exist in the TiO_2 films fabricated by the current PECVD process.[23] We notice that the intensities of both the PL subbands firstly increase from the in-glow discharge zone towards the boundary line, and then reduce at the afterglow zone. This phenomenon should be related to the plasma distribution and the system temperature as well. The boundary zone has the highest discharge temperature and is surrounded with a higher ion concentration, which finally leads to the thickest film and more opportunities for various lattice defects in the growth process. On the other hand, due to the excessive ion collisions, the film formed in the in-glow zone is too thin to emit intense light. Moreover, the obviously asymmetrical feature of the PL peaks suggests that more than one PL center should contribute to the broad band.[30] To clarify the origin of the broad band, each PL band is divided into two Gaussian subbands. A typical fitting result of spectrum d is shown as dashed lines in Fig. 4(a). The fitting results of all the spectra indicate that the two subbands are located at ~600 and ~680 nm, respectively. The integral area and the height of the subbands were recorded and their ratios between the two subbands were calculated and the results are plotted in Fig. 4(b). One can see that the ratios reach the maximum at spots d and e indicating the subband at shorter wavelength (subband 1) became weak in the boundary zone.

It has been reported in previous work that trapped holes like OVs tend to form on anatase nanoparticles, which will eventually lead to visible emission at a wavelength of around 600 nm.[23,31,32] In the present PECVD process, the precursor species aggregated into $(TiO_xCl_y)_n$ nanoparticles and rapidly nucleated into loosely packed web-like nanosized anatase nuclei.[33] In addition, this plasma system also provides a bipolar electric field, which could exert polarization assembly effects on the newly formed nanoparticle nuclei.[34] The active Cl^- rich environment and the assembly effects on the nanoparticles in the plasma bipolar electric field together lead to the self-confinement for the anatase TiO_2 sheet growth, causing more deficiencies in the newly formed crystal lattice and form

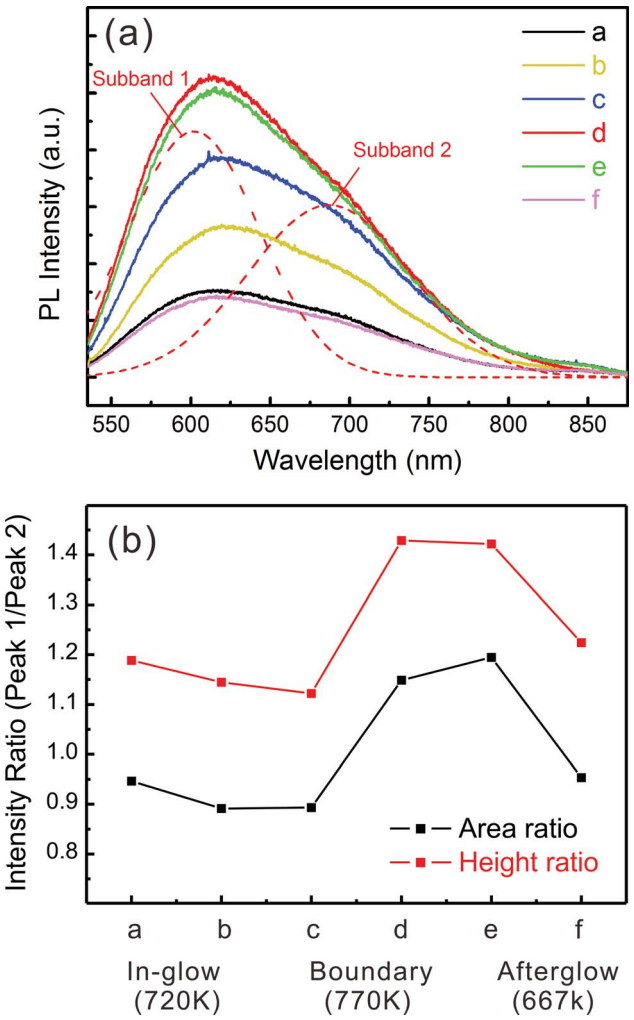

Fig. 4 (a) PL spectra from the as-prepared TiO_2 film corresponding to testing orientation of the test spots marked in Fig. 2(a). The dashed lines are the fitting curves (two Gaussian subbands) for the spectrum from spot d. (b) Integral area and height ratios of the two subbands for each of the six test spots (a–f).

electron scavengers such as OVs.[35–37] Thus we believe that the subband with shorter wavelength (subband 1) can be attributed to this lattice defect. Since the sheath region (the space between the two electrodes) of the reactor is only 0.57 mm, other effects of the discharge process such as the ion bombardment to the substrate are almost invisible.

In addition, electron traps were also demonstrated to dominate the emission spectrum of anatase TiO_2 crystals, exhibiting a PL peak at ~650 nm.[31] Detailed investigation ascribed this red PL to the radiative recombination of trapped electrons, about 0.7–1.6 eV below the conduction band edge, with valence band holes. It is not surprising that fitting peaks at similar wavelength (subband 2 in the current study) have also been detected in our case, which is especially likely to be caused by the existence of such electron traps. In the discharge process, the TiO_2 crystal growth is accompanied by self-release of ClO in the discharge atmosphere, which has been proved to have the ability to remove oxygen from the stoichiometric TiO_2 due to its

special recombination mechanism, and then subsequently introduce uncoordinated Ti atoms (*e.g.* Ti^{3+}) as electron traps without damaging the crystal regularity.[38]

To further prove the existence of both OVs and Ti^{3+} in our sample, we carried out XPS analyses (the measured area is 4 × 6 mm^2), and the results are plotted in Fig. 5. In the results of Ti2p (Fig. 5(a)), the peaks of $Ti^{4+}(2p_{3/2})$ and $Ti^{4+}(2p_{1/2})$ were confirmed with binding energy of 458.3 eV and 464.0 eV, which both have a visible red shift compared with the values from previous literature.[39,40] This phenomenon should be mainly attributed to the influence of uncoordinated Ti. It is reported that Ti^{3+} located with lower binding energy will exert a strong effect on the symmetric centre of the adjacent Ti^{4+} peaks, which will finally lead to this variation.[40,41] Besides, one can easily see from the XPS spectra that the O1s peak (Fig. 5(b)) has an asymmetric shape due to the effect of the defects. The peak was fitted and divided into two subbands, which correspond to Ti^{4+} and Ti^{3+}, respectively.[40] Both of the above features shown in Ti2p and O1s spectra suggest the existence of an OV–Ti^{3+} state.[42]

It is worth noting that the integral area and the height ratios of the two subbands are altered at different spots: subband 1 from OVs becomes stronger around the boundary zone. As discussed above, the film around the boundary zone is deposited at the highest temperature and this high temperature disturbs the lattice growth, enhancing the possibility of formation of OVs. Additionally, it should also be pointed out that the high temperature in this area can greatly influence the surface recombination coefficient of O or Cl through reactive release of ClO in our reaction system,[37] which will occupy an oxygen lattice site and is also believed to be a possible reason for the enhancement of OVs.[38] Since it has been reported that OVs are the most common defect related to lattice plane (101) and in view of the aforementioned XRD results, the increase of OVs in the boundary zone is not unexpected.[43]

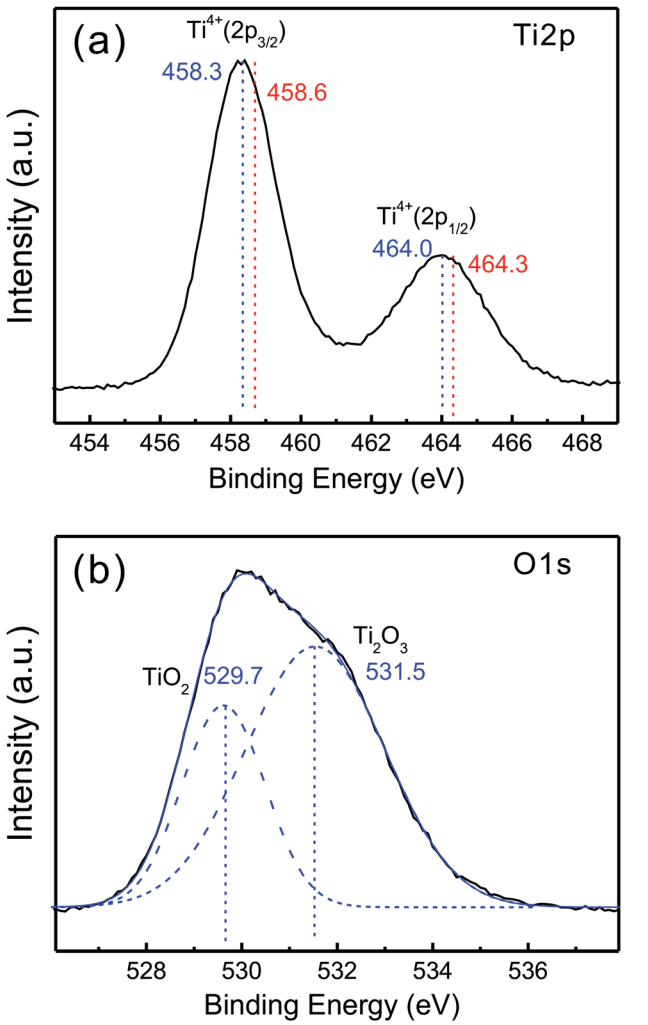

Fig. 5 XPS spectra of the TiO_2 film. (a) Ti2p. Comparisons were made between the standard value (red dashed lines) and measured value (blue dashed lines) in order to clarify the existence of oxygen vacancies and uncoordinated Ti. (b) O1s. The peak of O1s was fitted into two Gaussian subbands corresponding to Ti^{4+} and Ti^{3+}.

Conclusions

In summary, anatase TiO_2 films with different morphologies and controllable lattice orientation have been successfully fabricated on quartz substrate at atmospheric pressure by a PECVD process. Anatase films obtained in in-glow discharge zone and afterglow discharge zone exhibited various structural properties and were investigated in detail with microstructural characterizations, in which visible PL emission was detected as a result of various lattice defects. The temperature and the ion density in the deposition process are viewed as the main factors which finally determine the lattice structure and the defect properties of obtained anatase films. By changing the deposition parameters in the PECVD system, we should be able to selectively introduce lattice defects and efficiently modify the crystal structure in order to satisfy various demands in practical applications.

Acknowledgements

This work is supported by the Natural Science Foundation of China (nos 51322201, 11375042 and 51102049), "Shu Guang" project by Shanghai Municipal Education Commission and Shanghai Education Development Foundation, Project Based Personnel Exchange Program with CSC and DAAD, Specialized Research Fund for the Doctoral Program of Higher Education (no. 20120071110025), and Science and Technology Commission of Shanghai Municipality (nos 12520706300 and 12PJ1400500).

Notes and references

1 B. Oregan and M. A. Gratzel, *Nature*, 1991, **353**, 737.
2 M. Gratzel, *Nature*, 2001, **414**, 338.
3 A. Furube, T. Asahi, H. Masuhara, H. Yamashita and M. Anpo, *J. Phys. Chem. B*, 1999, **103**, 3120.
4 O. Yamamoto, K. Alvarez, T. Kikuchi and M. Fukuda, *Acta Biomater.*, 1999, **5**, 3605.

5 S. Gelover, L. A. Gomez, K. Reyes and M. T. Leal, *Water Res.*, 2006, **40**, 3274.
6 U. Diebold, N. Ruzycki, G. S. Herman and A. Selloni, *Catal. Today*, 2003, **85**, 93.
7 J. G. Yu, L. F. Qi and M. Jaroniec, *J. Phys. Chem. C*, 2010, **114**, 13118.
8 K. Zhu, N. R. Neale, A. Miedaner and A. J. Frank, *Nano Lett.*, 2007, **7**, 69.
9 D. Zhang, G. Li, H. Wang, K. M. Chan and J. C. Yu, *Cryst. Growth Des.*, 2010, **10**, 1130.
10 M. Lazzeri, A. Vittadini and A. Selloni, *Phys. Rev. B: Condens. Matter Mater. Phys.*, 2001, **63**, 155409.
11 W. S. Wang, D. H. Wang, W. G. Qu, L. Q. Lu and A. W. Xu, *J. Phys. Chem. C*, 2012, **116**, 19893.
12 Z. Zheng, B. Huang, X. Qin, X. Zhang, Y. Dai, M. Jiang, P. Wang and M. H. Whangbo, *Chem. – Eur. J.*, 2009, **15**, 12576.
13 H. Wang, J. Gao, T. Guo, R. Wang, L. Guo, Y. Liu and J. Li, *Chem. Commun.*, 2012, **48**, 275.
14 J. Miao and B. Liu, *RSC Adv.*, 2013, **3**, 1222.
15 T. R. Gordon, M. Cargnello, T. Paik, F. Mangolini, R. T. Weber, P. Fornasiero and C. B. Murray, *J. Am. Chem. Soc.*, 2012, **134**, 6751.
16 H. G. Yang, C. H. Sun, S. Z. Qiao, J. Zou, G. Liu, S. C. Smith, H. M. Cheng and G. Q. Lu, *Nature*, 2008, **453**, 638.
17 T. Ohsawa, M. A. Henderson and S. A. Chambers, *J. Phys. Chem. C*, 2010, **114**, 6595.
18 Y. He, O. Dulub, H. Cheng, A. Selloni and U. Diebold, *Phys. Rev. Lett.*, 2009, **102**, 106105.
19 H. Yanagi, S. Y. Chen, P. A. Lee, K. W. Nebesny, N. R. Armstrong and A. Fujishima, *J. Phys. Chem.*, 1996, **100**, 5447.
20 V. S. Lusvardi, M. A. Barteau, J. G. Chen, J. Eng, B. Fruhberger and A. Teplyakov, *Surf. Sci.*, 1998, **397**, 237.
21 A. J. Frank, N. Kopidakis and J. van de Lagemaat, *Coord. Chem. Rev.*, 2004, **248**, 1165.
22 J. Nisar, Z. Topalian, A. De Sarkar, L. Osterlund and R. Ahuja, *ACS Appl. Mater. Interfaces*, 2013, **5**, 8516.
23 M. L. Li, G. S. Huang, Y. Q. Qiao, J. Wang, Z. Q. Liu, X. Y. Liu and Y. F. Mei, *Nanotechnology*, 2013, **24**, 305706.
24 R. Wang, K. Hashimoto, A. Fujishima, M. Chikuni, E. Kojima, A. Kitamura, M. Shimohigoshi and T. Watanabe, *Adv. Mater.*, 1998, **10**, 135.
25 G. M. Wang, H. Y. Wang, Y. C. Ling, Y. C. Tang, X. Y. Yang, R. C. Fitzmorris, C. C. Wang, J. Z. Zhang and Y. Li, *Nano Lett.*, 2011, **11**, 3026.
26 D. Zhang, G. Li, X. Yang and J. C. Yu, *Chem. Commun.*, 2009, 4381.
27 S. D. Burnside, V. Shklover, C. Barbe, P. Comte, F. Arendse, K. Brooks and M. Gratzel, *Chem. Mater.*, 1998, **10**, 2419.
28 Y. Dai, C. M. Cobley, J. Zeng, Y. Sun and Y. Xia, *Nano Lett.*, 2009, **9**, 2455.
29 L. Qian, Z. S. Jin, S. Y. Yang, Z. L. Du and X. R. Xu, *Chem. Mater.*, 2005, **17**, 5334.
30 G. S. Huang, X. L. Wu, Y. F. Mei, X. F. Shao and G. G. Siu, *J. Appl. Phys.*, 2003, **93**, 582.
31 C. C. Mercado, F. J. Knorr, J. L. McHale, S. M. Usmani, A. S. Ichimura and L. V. Saraf, *J. Phys. Chem. C*, 2012, **116**, 10796.
32 C. C. Mercado, F. J. Knorr and J. L. McHale, *ACS Nano*, 2012, **6**, 7270.
33 C. Lazzaroni, P. Chabert, M. A. Lieberman, A. J. Lichtenberg and A. Leblanc, *Plasma Sources Sci. Technol.*, 2012, **21**, 035013.
34 Q. Y. Yang, D. X. Wang, Y. Guo, K. Ding, J. Z. Xu, J. J. Shi and J. Zhang, *J. Phys. D: Appl. Phys.*, 2011, **44**, 5.
35 Z. Zhang and J. T. Yates, Jr, *J. Phys. Chem. Lett.*, 2010, **1**, 2185.
36 K. Yamada, H. Yamane, S. Matsushima, H. Nakamura, T. Sonoda, S. Miura and K. Kumada, *Thin Solid Films*, 2008, **516**, 7560.
37 E. G. Thorsteinsson and J. T. Gudmundsson, *Plasma Sources Sci. Technol.*, 2010, **19**, 015001.
38 E. McCafferty, *Corros. Sci.*, 1995, **37**, 481.
39 M. Xing, W. Fang, M. Nasir, Y. Ma, J. Zhang and M. Anpo, *J. Catal.*, 2013, **297**, 236.
40 X. Zhang, H. Tian, X. Wang, G. Xue, Z. Tian, J. Zhang, S. Yuan, T. Yu and Z. Zou, *Mater. Lett.*, 2013, **100**, 51.
41 F. Guillemot, M. C. Porte, C. Labrugere and C. Baquey, *J. Colloid Interface Sci.*, 2002, **255**, 75.
42 Y. Yu, K. Wu and D. Wang, *Appl. Phys. Lett.*, 2011, **99**, 192104.
43 D. J. Kim, S. I. Pyun and Y. G. Yoon, *J. Alloys. Compd.*, 1996, **235**, 182.